

# Carbonate-Hydroxide Induced Metal-Organic Framework Transformation Strategy for Honeycomb-Like NiCoP Nanoplates to Drive Enhanced pH-Universal Hydrogen Evolution

Lin Zhang, Fei Ye, Zeyi Wu, Le Jiang, Qiang Liu, Ruilvjing Pang, Yang Liu, and Linfeng Hu\*

Developing a low-cost, pH-universal electrocatalyst is desirable for electrochemical water splitting but remains a challenge. NiCoP is a promising non-noble hydrogen-evolving electrocatalyst due to its high intrinsic electrical conductivity, fast mass transfer effects, and tunable electronic structure. Nevertheless, its hydrogen evolution reaction (HER) activity in full pH-range has been rarely developed. Herein, a Ni–Co carbonate-hydroxide induced metal-organic framework transformation strategy is proposed to in situ grow porous, honeycomb-like NiCoP nanoplates on Ni foam for high-performance, pH-universal hydrogen evolution reaction. The resultant NiCoP catalyst exhibits a highly 2D nanoporous network in which 20–50 nm, well-crystalline nanoparticles are interconnected with each other closely, and delivers versatile HER electroactivity with  $\eta_{10}$  of 98, 105, and 97 mV in 1 M KOH, 0.5 M H<sub>2</sub>SO<sub>4</sub>, and 1 M phosphate buffer solution electrolytes, respectively. This overpotential remarkably surpasses the one of commercial Pt/Cs in both neutral and alkaline media at a large current density (>100 mA cm<sup>-2</sup>). The corresponding full water-splitting electrolyzer constructed from the 2D porous NiCoP cathode requires only a cell voltage of 1.43 V at 10 mA cm<sup>-2</sup>, superior to most recently reported electrocatalysts. This work may open up a new avenue on the rational design of nonprecious, pH-universal electrocatalyst.

the hydrogen evolution reaction (HER), capable of working with greater efficiency irrespective of pH value.<sup>[6–8]</sup> Unfortunately, the scarcity and cost of precious Pt greatly restrict its industrial commercialization. Seeking transition-metal-based electrocatalysts with cost-effective, earth-abundant, high-efficiency, and good durability thus is highly desirable to expedite global scalability of hydrogen energy applications.<sup>[9–11]</sup>

Most recently, transition metal phosphides (TMPs) have been widely explored for catalyzing the HER and oxygen evolution reaction (OER). Among them, NiCoP has been attracted significant attention due to their high intrinsic electrical conductivity, fast mass transfer effects, and tunable electronic structure.<sup>[12–14]</sup> Especially, its high resistant of corrosion results in excellent chemical stability, making it as promising candidate for electrolytic pH-universal HER. Nevertheless, its HER activity suffers from unfavorable geometric structures with limited charge transfer capability and lack of exposed active sites,<sup>[15–17]</sup>

## 1. Introduction

The electrochemical water splitting driven by renewable energy sources, such as solar and wind power, has been regarded as the optimal route for sustainable hydrogen production.<sup>[1–5]</sup> Water dissociation for hydrogen production via electrolysis requires highly active catalysts to minimize overpotentials. Currently, Pt-based catalysts are still the pioneering ones in catalyzing

resulting in a high overpotential (>120 mV vs reversible hydrogen electrode (RHE)) to attain the standard current density of 10 mA cm<sup>-2</sup> compared to Pt-based catalyst counterparts.

It is known that 2D nanomaterials (nanosheets, nanoflakes, and nanoplates) with micrometer-sized lateral surface and thin thickness are attracting increasing attention on HER electrocatalysis owing to their intriguing physicochemical properties such as the strong in-plane covalent bond and high exposure of surface atoms allows easy regulation to the properties and functionalities.<sup>[18–20]</sup> Furthermore, if one can construct a large number of nanopores on the 2D nanostructure surface or inside, there is no doubt that electrocatalysis performance should be significantly enhanced owing to the greatly exposed active surface, the rapid diffusion of electrolyte and the rapid release of formed H<sub>2</sub> and O<sub>2</sub> from the catalyst surface.<sup>[21–23]</sup> Recently, 2D NiCoP nanosheets with high porosity, larger specific surface area has been developed using various synthetic routes with superior catalytic activity on water splitting.<sup>[24–26]</sup> However, most of the as-developed NiCoP nanosheets just exhibit excellent HER catalytic activity toward in alkaline media, and its pH-universal HER performance has been rarely

L. Zhang, Z. Y. Wu, L. Jiang, L. F. Hu

Department of Materials Science

Fudan University

Shanghai 200433, P. R. China


F. Ye, Q. Liu, R. L. J. Pang, Y. Liu, L. F. Hu

School of Materials Science and Engineering

Southeast University

Nanjing 211189, P. R. China

E-mail: linfenghu@seu.edu.cn

 The ORCID identification number(s) for the author(s) of this article can be found under <https://doi.org/10.1002/smtd.202200515>.

DOI: 10.1002/smtd.202200515

developed.<sup>[27,28]</sup> Generally, the HER performance in neutral environment is inferior to that in the alkaline/acid condition. Due to the large ohmic loss and the low proton concentration, the HER proceeding in a neutral medium exhibits much slower kinetics compared to that in alkaline or acidic conditions.<sup>[29]</sup> It is of great interest to realize the enhancement of pH-universal HER performance of NiCoP catalyst.

Metal-organic frameworks (MOFs) are an important category of porous materials with ultrahigh porosity and surface areas extending beyond 6000 m<sup>2</sup> g<sup>-1</sup>, which has been widely used as the precursor on the designing inorganic porous or core-shell structures.<sup>[30]</sup> Most recently, Ma et al. have reported a topology-guided bottom-up synthesis of hexagonal 2D MOF nanoplate with lateral size of ≈800 nm and thickness less than 20 nm.<sup>[31]</sup> Such a synthetic progress inspires us to consider the possible preparation of porous 2D NiCoP nanostructures from these 2D MOF precursors. Inspired this consideration, we developed a Ni-Co carbonate-hydroxide (NCCH) induced 2D MOF transformation strategy to in-situ grow 10–40 nm porous, honeycomb-like NiCoP nanoplates on Ni foam for high-performance, pH-universal hydrogen evolution reaction. In our strategy, NCCH seed plays a key role in the NiCoP phase formation as Co species supplement source, and Ni-MOF precursor contributes to the production of high porosity. The resultant NiCoP catalyst exhibits a 2D honeycomb-like network in which 20–50 nm, well-crystalline nanoparticles were interconnected with each other closely. Prominent pH-universal HER performance with overpotentials of 98, 105, and 97 mV in 1 M KOH, 0.5 M H<sub>2</sub>SO<sub>4</sub> and 1 M phosphate buffer solution (PBS) at the current density of 10 mA cm<sup>-2</sup> has been achieved, respectively. The corresponding full water-splitting electrolyzer constructed from the 2D nanoporous NiCoP cathode requires a cell voltage of 1.43 V at 10 mA cm<sup>-2</sup> in alkaline media with a low overpotential of 202 mV.

## 2. Results and Discussion

### 2.1. Synthesis and Structural Characterization

Honeycomb-like NiCoP nanoplates were prepared via a two-step hydrothermal route followed by a low-temperature phosphorization process (Figure 1a). First, we realize an in-situ growth of basic carbonate nanoplate arrays on Ni foam substrate. X-ray diffraction (XRD) (Figure S1, Supporting Information) pattern of the as-grown basic carbonate indicates an orthorhombic NiCo<sub>2</sub>(CO<sub>3</sub>)<sub>1.5</sub>(OH)<sub>3</sub> (NCCH, JCPDS 48–0083) phase with high purity.<sup>[28]</sup> Scanning electron microscopy (SEM) observation confirms a highly dense coverage of the Ni foam with the NCCH nanoplates. Considering the large size with a lateral length of ≈2 μm is beneficial to its use as a support, we tried to further grow Ni-MOF on these 2D NCCH seed layers. With a pyridine-assisted, bottom-up method as reported previously,<sup>[32]</sup> the 2D hexagonal Ni-MOF nanoplates were successfully deposited on the NCCH templates with an apparent color change from pink to light green (Figure S3, Supporting Information). In such a second growth process, a pair of Ni<sup>2+</sup> cations are coordinated with eight oxygen atoms from four BDC anions to form a paddle wheel secondary building unit (SBU) and then connected via DABCO molecules through the terminal nitrogen atoms. The diffraction peaks in range of 5°–10° match well with those of Ni-MOF (Figure 1b). The

Fourier transform infrared (FTIR) spectra of Ni-MOF, NCCH and Ni-MOF@NCCH (MOF/NiCo) are shown in Figure 1c. In Ni-MOF@NCCH IR spectra, the discernible peak in 1618 cm<sup>-1</sup> is corresponding to the stretching modes of C–N of Ni-MOF, respectively.<sup>[33]</sup> Besides, the bands around 620 cm<sup>-1</sup> are ascribed to δ<sub>OH</sub> vibrations of NCCH respectively.<sup>[34]</sup> Raman has also shown the presence of characteristic peaks of Ni-MOF in Ni-MOF@NCCH. Typical Raman peaks in 1426 and 1600 cm<sup>-1</sup> originating from the vibrational modes from organic component of the Ni-MOF are detected in Ni-MOF@NCCH.<sup>[35]</sup> And the peaks in 467 cm<sup>-1</sup> originating from the polarized A<sub>1g</sub> mode of the Ni(Co)-O modes of the NCCH are also detected in Ni-MOF@NCCH.<sup>[36]</sup> SEM and transmission electron microscopy (TEM) observation reveals a uniform growth of Ni-MOF with a lateral size of about 1.5 μm on the NCCH seed (Figure 1f,g, Figure S4, Supporting Information). The corresponding X-ray energy-dispersive spectroscopy (EDS) elemental mapping taking from an assembly of Ni-MOF@NCCH (MOF/NiCo) structure verified the uniform distribution of Ni, O elements in the Ni-MOF and also of Co, Ni elements in NCCH seed.

Subsequently, 10–40 nm porous honeycomb-like NiCoP nanoplates can be formed through a controlled treatment of Ni-MOF@NCCH@Ni precursors by a low-temperature phosphorization at 325°C using NaH<sub>2</sub>PO<sub>4</sub> as phosphorus source. During the process, the decomposition of NaH<sub>2</sub>PO<sub>4</sub> release PH<sub>3</sub> source, and the color of Ni-MOF@NCCH@Ni foam changed from light green to black (Figure S3, Supporting Information), suggesting the possible formation of metal phosphides (named as MOF/NiCo-325 below). As confirmed by the XRD characterization, the diffraction peaks of Ni-MOF and NCCH seed completely disappeared after phosphorization. Instead, diffraction peaks located at 40.9, 44.8, 44.5, 47.5, 54.4, and 54.7 appeared, which can be indexed to the (1 1 1), (2 0 1), (2 1 0), (3 0 0), and (0 0 2) planes of NiCoP phase (JCPDS no. 71–2336), respectively. SEM and TEM images of the phosphorization product show 2D nanoplate structure with abundant pores with a size of 10–40 nm (Figure 2b–e). In detail, SEM and TEM observations demonstrate ≈1.5 μm, well-defined hexagonal shaped plates with rather rough surface (Figure 2b). The thickness of the plates can be determined to ≈300 nm by magnified SEM image inserted in Figure 2b. TEM observation further confirms a 2D honeycomb-like network in which 20–50 nm, well-crystalline nanoparticles were interconnected with each other closely (Figure 2c,d). These exposed active surfaces are expected to create more accessible active sites and provide multiple pathways for the mass transfer, which is in favor of the solution-phased HER. The influence of phosphorization process on the mesoporous formation was further studied. Figure S5 (Supporting Information) shows the SEM images of NiCoP samples prepared at various phosphorization times. When the calcination time was less than 10 min, the initial Ni-MOF@NCCH morphology is generally lost and transformed into hexagonal nanoplates with rather rough surface. However, no nanopores were observed at this stage. When the phosphating time prolonged to 65 min, a large number of nanopores emerged on the surface. We speculated that the mass transfer between Ni-MOF and NCCH/NF occurred during the calcination process, and some components volatilized simultaneously to form abundant nanopores. High-resolution TEM (HRTEM) observation clearly exhibits an interplanar spacing of 0.50 nm, corresponding to

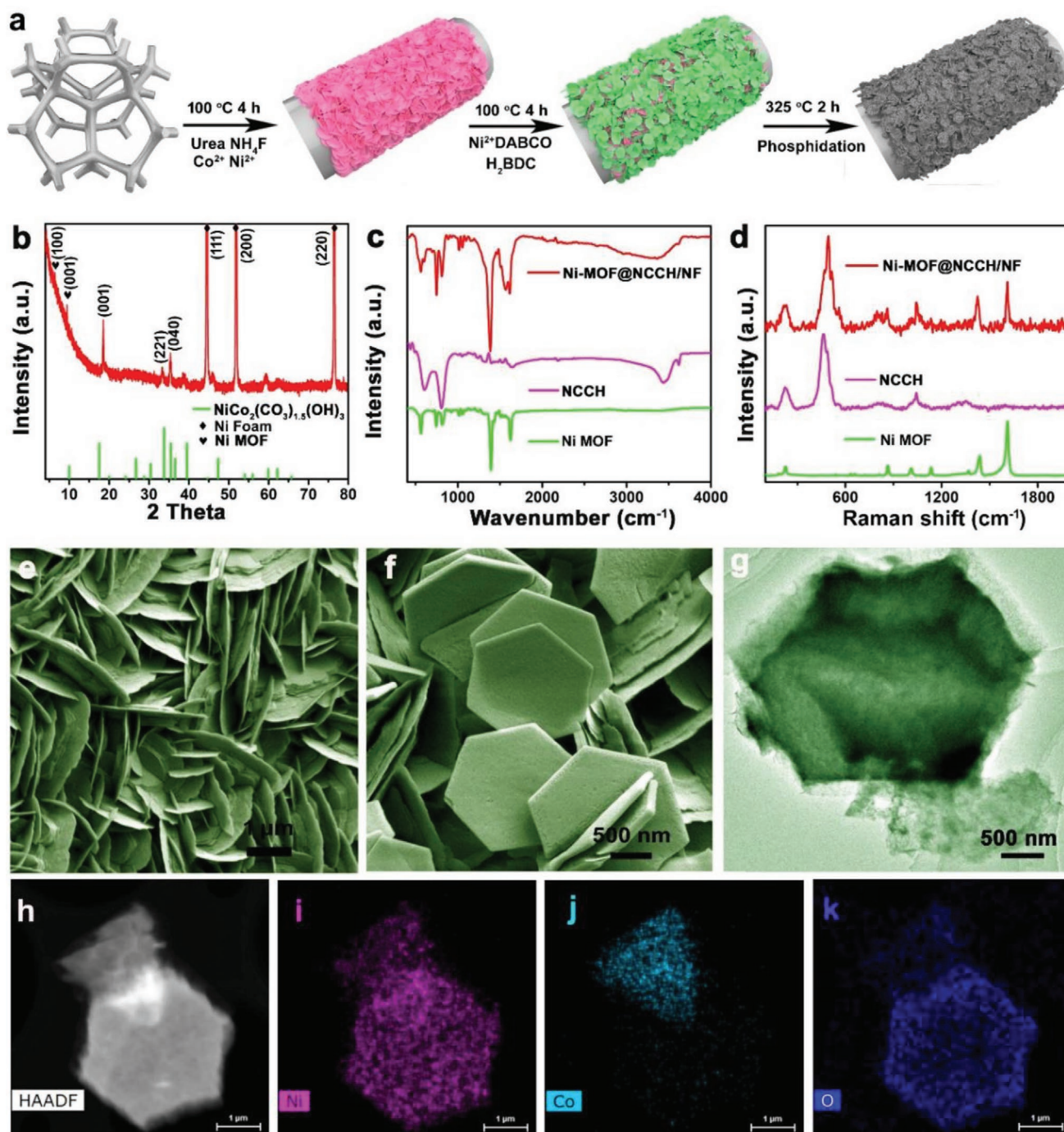


**Figure 1.** a) Schematic illustration of the routes to MOF/NiCo-325. b) XRD pattern of MOF/NiCo and c,d) Raman spectra and FTIR spectra of Ni-MOF, NCCH seed layer and Ni-MOF@NCCH (MOF/NiCo). e,f) Typical SEM images of NCCH layer and Ni-MOF@NCCH (MOF/NiCo). g) TEM images and h–k) EDS Elemental mapping of Ni, Co, O, elements of Ni-MOF@NCCH (MOF/NiCo) on Ni Foam.

the (1 0 1) plane of NiCoP. Selected area electron diffraction (SAED) pattern in Figure 2e shows typical polycrystalline rings. X-ray energy-dispersive spectroscopy (EDS) elemental mapping of the porous MOF/NiCo-325 verified the uniform distribution of Ni, Co and P elements in the hexagon nanoplate, suggesting that a portion of Co species was transferred from NCCH seed into the Ni-MOF during the phosphorization (Figure 2g,j).

The role of NCCH seed layer and MOF precursor on the porous NiCoP formation was further examined under the similar synthetic condition but remove such a layer. As a result, Ni<sub>2</sub>P (noted as Ni-325 sample below) phase with irregular morphology was obtained without NCCH seed (Figure S6a–c, Supporting Information), suggesting NCCH plays a key role in the NiCoP phase formation as Co species supplement source

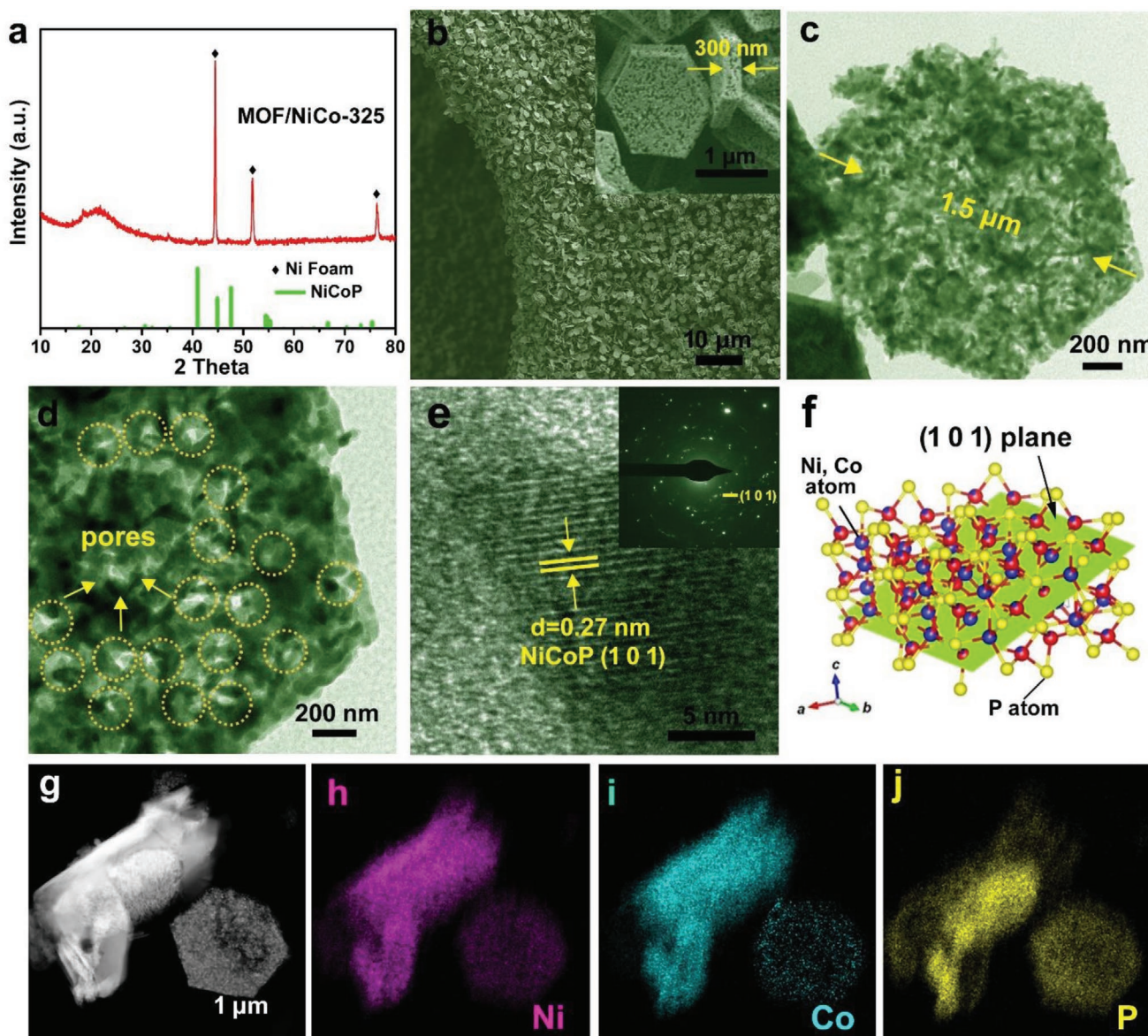


**Figure 2.** a) Typical XRD pattern, b–e) SEM, TEM, and HRTEM images of MOF/NiCo-325 with the corresponding SAED pattern inserted. f) Schematic illustration of the crystallographic configuration of NiCoP (101) plane. g–j) EDS elemental mapping of Ni, Co, P, elements.

during the phosphorization process.<sup>[37]</sup> On the other hand, the sample directly calcined sample from NCCH with the absence of Ni-MOF (noted as NiCo-325 below) shows very smooth surface with the absence of abundant nanopores (Figure S6d–f, Supporting Information). These results identified Ni-MOF precursor that contributes to the production of high porosity of our NiCoP sample.

## 2.2. Electrocatalytic Performance

HER performance of the resultant MOF/NiCo-325@Ni sample was then evaluated by linear sweep voltammetry (LSV) in 1.0 M KOH solution. The activities of Ni-325, NiCo-325 and commercial Pt/C (20% Pt) counterparts were also measured as

comparison. All polarization curves of samples were collected with 90% IR correction. MOF/NiCo-325 catalyst displays excellent HER activity with an overpotentials of 98 and 148 mV to achieve the current density of 10 and 100 mA cm<sup>-2</sup>, respectively, which is much lower than those of Ni-325 (194 and 302 mV), NiCo-325 (125 and 218 mV) (Figure 3a). Note that the value of  $\eta_{10}$  for MOF/NiCo-325 is also lower than the corresponding values for most of the recently reported electrocatalysts (Table S3, Supporting Information). Its activity is even higher than that of Pt/C at a large current density (>140 mA cm<sup>-2</sup>). The Tafel slope of MOF/NiCo-325 is 48 mV dec<sup>-1</sup>, which is smaller than that of Ni-325 (118 mV dec<sup>-1</sup>) and NiCo-325 (86 mV dec<sup>-1</sup>), demonstrating more rapid reaction kinetics of our MOF/NiCo-325 (Figure 3b). Such a Tafel slope suggests that the HER route of MOF/NiCo-325 follows the Volmer–Heyrovsky mechanism and

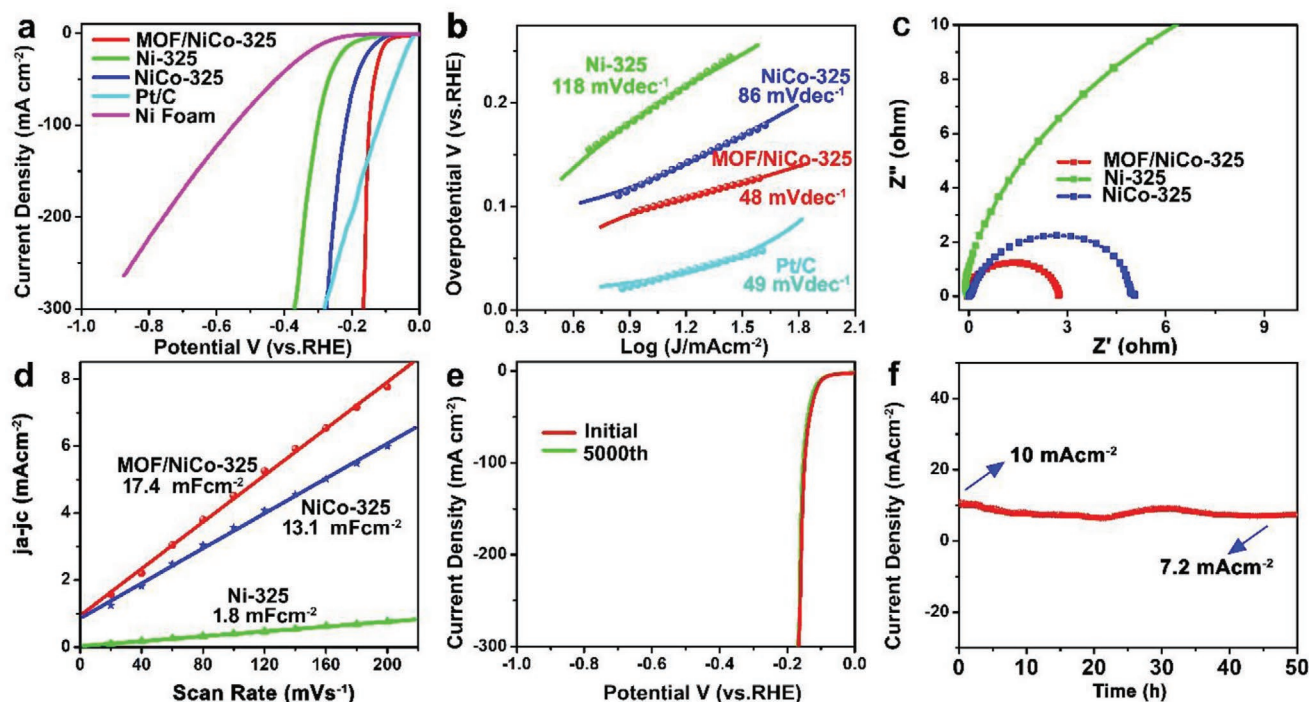


**Figure 3.** a) LSV curves with 90%  $iR$ -corrections for MOF/NiCo-325, Ni-325, NiCo-325, Pt/C, and Ni foam for the HER in 1 M KOH. b,c) Tafel slope and Nyquist plots of MOF/NiCo-325, Ni-325, and NiCo-325. d) The measured capacitive current density at  $-0.015$  V as a function of the scan rate for MOF/NiCo-325, Ni-325, NiCo-325. e) Polarization curves for MOF/NiCo-325 before and after 5000 cycles for HER. f)  $I-t$  curve for MOF/NiCo-325 at the  $\eta_{10}$  for 50 h.

the electrochemical desorption of hydrogen is the rate-limiting step.<sup>[38]</sup> Electrochemical impedance spectroscopy (EIS) test was performed to further understand the underlying mechanism for the enhanced HER activity. In accordance with the order of HER activity, MOF/NiCo-325 has the smallest semicircle among all the tested electrodes, indicating its low charge transfer resistance ( $R_{ct}$ ) at the electrode/electrolyte interface, which is attributed to the combination effects of the enhanced conductivity of the porous nanoplate layer and rapid electron transfer of the MOF/NiCo-325 catalyst. Additionally, the electrochemical double layer capacitance ( $C_{dl}$ ) of an electrocatalyst is proportional to its electrochemically active surface area (ECSA).<sup>[39]</sup> The  $C_{dl}$  of MOF/NiCo-325, NiCo-325, Ni-325 are estimated as 17.4, 13.1, and 1.8  $\text{mF cm}^{-2}$ , respectively (Figure 3d, Figure S7, Supporting Information). Such a high  $C_{dl}$  value suggests that the porous MOF/NiCo-325 sample affords more exposed active sites for high catalytic efficiency. In order to further understand the intrinsic activity, the turnover frequency (TOF) of HER normalized to the number of active sites was estimated, as shown in Figure S8 (Supporting Information). The MOF/NiCo-325 catalyst also delivers the highest TOF of  $4.08 \text{ s}^{-1}$  per site at overpotential of 150 mV, which is larger than that of Ni-325 ( $0.79 \text{ s}^{-1}$ ) and NiCo-325 ( $1.32 \text{ s}^{-1}$ ). The high TOF value of MOF/NiCo-325 is well agreement with its excellent activity toward the HER.

Apart from the catalytic activity, the long-term durability is another important factor for the catalyst. The working electrode was handled for 5000 cycles using a continuous cyclic voltammetry measurement between 0 and  $-0.4$  V (vs RHE). As shown in Figure 3e, the polarization curves of MOF/NiCo-325 catalyst before and after 5000 cyclic voltammetry (CV)

test nearly overlap with each other, especially at the low overpotential region. In addition, the chronoamperometric ( $I-t$ ) measurement illustrates that the current density shows a slight decline (almost 72% remained) over the duration of 50 h, demonstrating the outstanding HER stability of MOF/NiCo-325 in alkaline media. Then, XRD, SEM, and X-ray photoelectron spectra (XPS) measurements were carried out to identify the phase evolution of the porous NiCoP during the HER process. As shown in Figures S9 and S10 (Supporting Information), the crystal structure and morphology of MOF/NiCo-325 are well maintained after HER. All of the above reasons contribute to the prominent stability of the MOF/NiCo-325 electrocatalyst.

Known that most of the transition-metal phosphide catalysts reported to date are only suitable for the HER at a specific pH value, and Pt as the state-of-art HER catalyst in acidic media also exhibits 2 or 3 orders of magnitude lower activity when operated in alkaline or neutral media.<sup>[40]</sup> Considering a nonprecious pH-universal HER electrocatalyst is highly desirable for hydrogen production,<sup>[40,41]</sup> HER performance of MOF/NiCo-325 electrocatalysts were examined in different pH-valued electrolytes including 1 M KOH, 1 M PBS, and 0.5 M  $\text{H}_2\text{SO}_4$ . Figure 4a shows the polarization LSV curves of different electrodes in the 0.5 M  $\text{H}_2\text{SO}_4$ . Obviously, the MOF/NiCo-325 nanoplate exhibits the best activity with low overpotentials of  $\eta_{10} = 105$  and  $\eta_{100} = 158$  mV, much lower than those of Ni-325 (312 and 474 mV), NiCo-325 catalysts (156 and 301 mV) and other reported catalysts (Table S5, Supporting Information). The Tafel slope of MOF/NiCo-325 is  $50 \text{ mV dec}^{-1}$ , which is smaller than that of Ni-325 ( $185 \text{ mV dec}^{-1}$ ) and NiCo-325 ( $86 \text{ mV dec}^{-1}$ ), demonstrating a more rapid reaction kinetics of MOF/NiCo-325

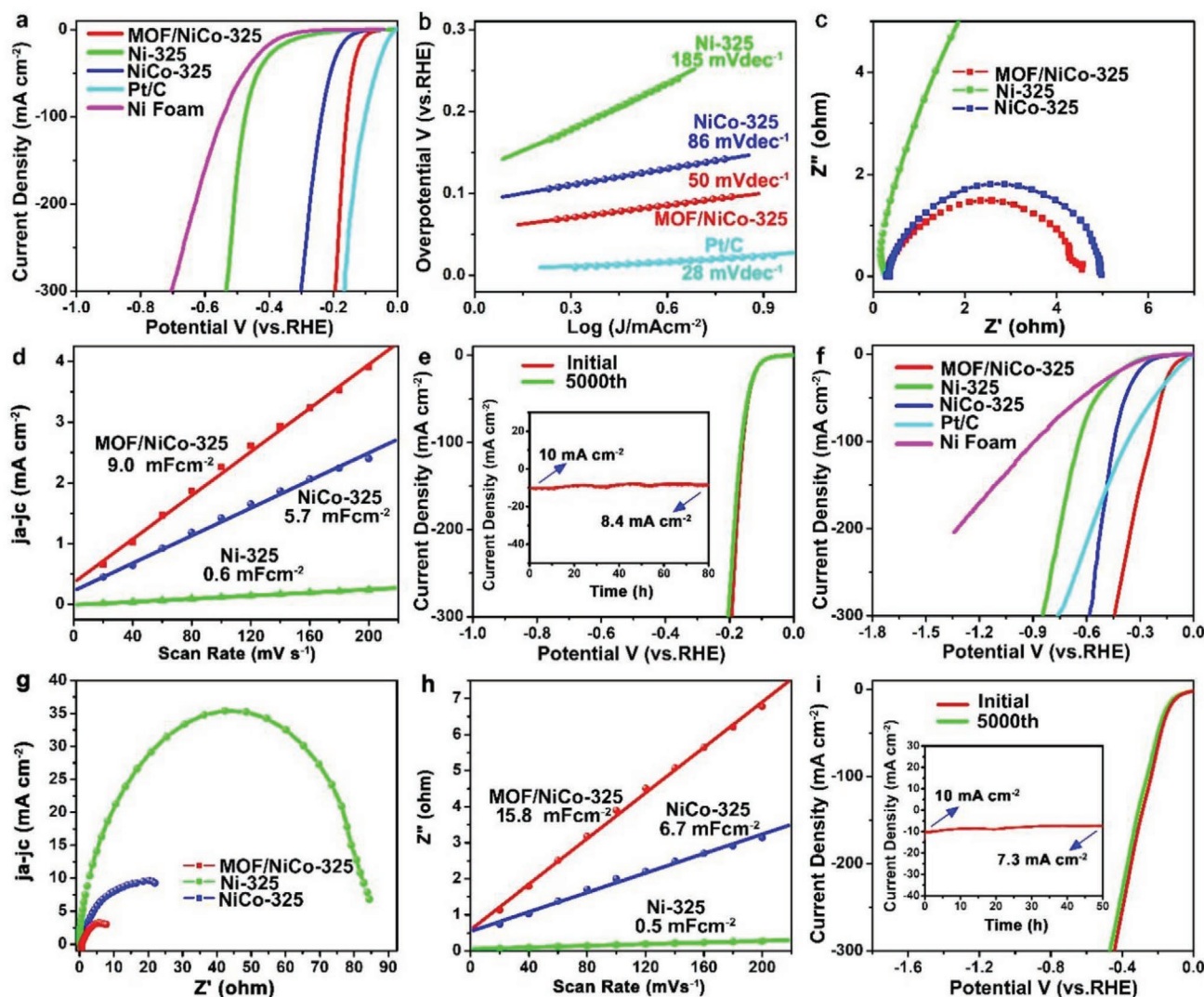


**Figure 4.** Polarization curves and for commercial Pt/C, MOF/NiCo-325, Ni-325, and NiCo-325 in a) 0.5 m H<sub>2</sub>SO<sub>4</sub> and f) 1 m PBS electrolytes, respectively. b). Tafel slope of Pt/C, MOF/NiCo-325, Ni-325, and NiCo-325 in 0.5 m H<sub>2</sub>SO<sub>4</sub>. Nyquist plots of MOF/NiCo-325, Ni-325, and NiCo-325 catalysts in c) 0.5 m H<sub>2</sub>SO<sub>4</sub> and g) 1 m PBS electrolytes, respectively. The measured capacitive current density at 0.02 V as a function of the scan rate for MOF/NiCo-325, Ni-325, and NiCo-325 in d) 0.5 m H<sub>2</sub>SO<sub>4</sub> and h) 1 m PBS electrolytes, respectively. Polarization curves of MOF/NiCo-325 before and after 5000 CV cycles test at e) 0.5 m H<sub>2</sub>SO<sub>4</sub> and i) 1 m PBS. Inset: the current–time (*I*–*t*) curves of MOF/NiCo-325 catalyst for 50 h.

(Figure 4b). The low Tafel slope indicates that MOF/NiCo-325 catalyst follows a Volmer–Heyrovsky mechanism in the acid solution. EIS measurements also imply the fastest charge transfer of the MOF/NiCo-325 catalyst than Ni-325 and NiCo-325 occurs during the HER process. This should be attributed to the combination function of the increased conductivity of the Ni Foam and rapid electron transfer of the porous NiCoP nanoplate (Figure 4c). The  $C_{dl}$ 's value for the MOF/NiCo-325 nanoplates, Ni-325, and NiCo-325 is 9.0, 0.6, and 5.7 mF cm<sup>-2</sup>, respectively (Figure 4d, Figure S11, Supporting Information). The larger  $C_{dl}$  values suggested the important role of the porous nanoplate in improving the catalytic activity. In addition, the long-term CV cycling and *I*–*t* test suggest that the MOF/NiCo-325 catalyst also possesses superior stability in a long-term electrochemical process in 0.5 m H<sub>2</sub>SO<sub>4</sub> (Figure 4e). As shown in Figures S12 and S13 (Supporting Information),

the diffraction peaks of the sample after the long-term CV cycling for HER are similar to the original MOF/NiCo-325 (Figure 2a), indicating that the phase structure was well maintained and the HER activity comes from the NiCoP catalyst. The activity trend of the catalysts in 1 m PBS is the same as that tested in alkaline and H<sub>2</sub>SO<sub>4</sub> electrolytes. As displayed in Figure 4f,i, the MOF/NiCo-325 sample respectively exhibits  $\eta_{10} = 97$  and  $\eta_{100} = 239$  mV in this neutral media, which is much lower than those of Ni-325 (348 and 644 mV) and NiCo-325 catalysts (261 and 445 mV), respectively. It is noteworthy that this overpotential obtained in neutral media is much lower than that of other NiCoP catalysts as reported previously (Table S7, Supporting Information), and also comparable to most of the recently HER electrocatalysts in 1 m PBS (Table S8, Supporting Information). The corresponding Tafel slopes of the MOF/NiCo-325, Ni-325 and NiCo-325 catalysts are 87, 176 and

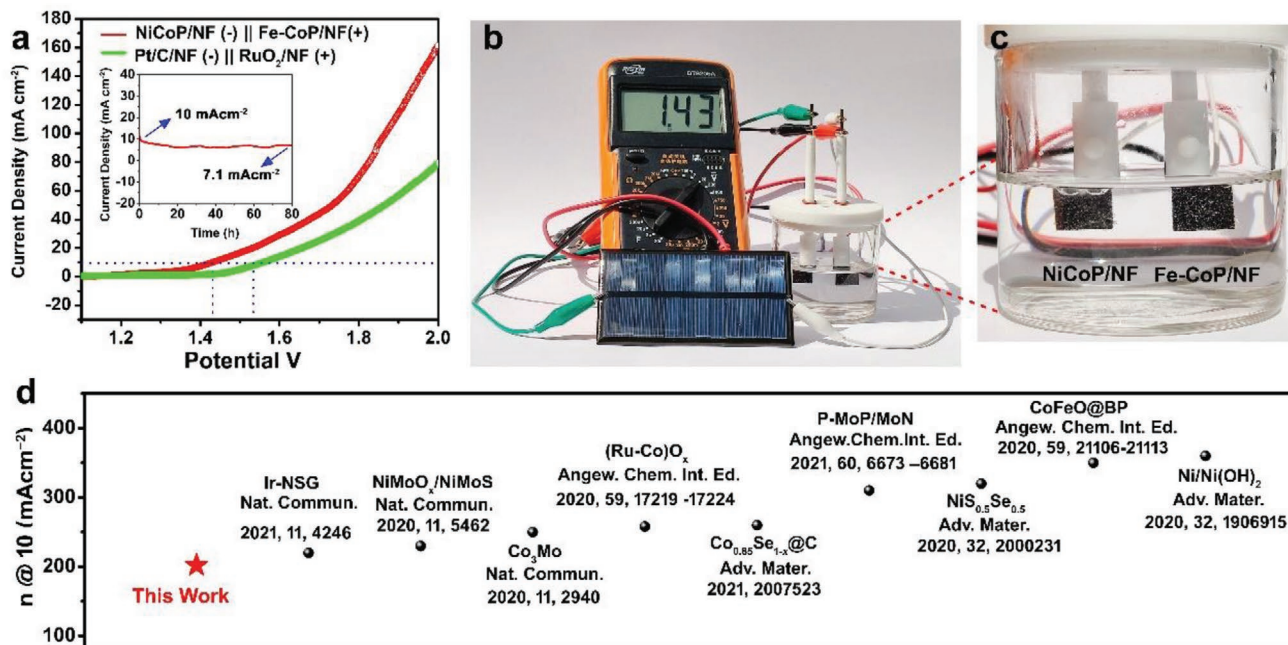


**Figure 5.** a) Polarization curves for NiCoP/NF(-) || Fe-CoP/NF(+) and Pt/C/NF(-) || RuO<sub>2</sub>/NF(+) for overall water splitting in 1 M KOH (two-electrode structure). Inset: *I-t* curve of NiCoP/NF || Fe-CoP/NF for 80 h. b, c) Photograph of a water-splitting device driven by a solar cell (≈1.43 V) and photograph showing the generation of O<sub>2</sub> and H<sub>2</sub> bubbles on the surface of MOF/NiCo-325. d) Comparison with state-of-the-art water splitting electrocatalysts.

147 mV dec<sup>-1</sup> (Figure S14, Supporting Information). The low Tafel slope indicates that MOF/NiCo-325 catalyst also follows a Volmer–Heyrovsky mechanism in the neutral solution.<sup>[44]</sup> The *C<sub>dl</sub>* value of MOF/NiCo-325 is 15.8 mF cm<sup>-2</sup>, also larger than those of Ni-325 (6.7 mF cm<sup>-2</sup>) and NiCo-325 (0.5 mF cm<sup>-2</sup>) samples (Figure S15, Supporting Information). Besides the high activity, our MOF/NiCo-325 sample also show excellent negligible activity decay after 5000 continuous cycling test and long-term stability over 50 h by chronopotentiometry test in 1 M PBS with well retaining the initial morphology and phase structure (Figures S16 and S17, Supporting Information).

We consider the superior electrocatalytic performance in the wide pH range should be ascribed to the unique structure of our NiCoP electrocatalyst: i) First, this honeycomb-like nanoplate with high porosity increases numerous active sites, enhances the contact between the electrolyte and catalyst and promotes the desorption of the as-generated H<sub>2</sub> from the electrocatalyst surface. ii) Second, a part of Co transfers from NCCH seed to Ni-MOF derivatives during phosphating, regulating the electron donor-acceptor behavior for an improved catalytic activity. As confirmed by XPS characterization in Figure S19 (Supporting Information), the binding energy of Ni and P in MOF/NiCo-325 is positively shifted about 0.9 eV compared with that in Ni<sub>2</sub>P. The result indicates the changes of local electronic density around Ni sites by the incorporation of Co.<sup>[42]</sup> iii) Third, the close contact between NiCoP and the Ni foam substrate significantly facilitates the rapid transfer of electrons during hydrogen evolution reaction.

Finally, we tried to couple our MOF/NiCo-325 electrocatalyst with suitable OER catalyst to realize overall water splitting. Fe-CoP/NF catches our attention as OER electrocatalyst owing to its remarkable activity with a low potential of 295 mV to

reach 500 mA cm<sup>-2</sup> in the alkaline electrolyte.<sup>[43]</sup> As depicted in Figure 5a, the polarization curve shows the good activity of the MOF/NiCo-325(-) || Fe-CoP(+) electrolyzer for overall water splitting with an overpotential of 200 mV and a low cell voltage of 1.43 V to derive a current density of 10 mA cm<sup>-2</sup>, which is superior to that of Pt/C/NF(-) || RuO<sub>2</sub>/NF(+) electrolyzer (1.56 V). For the practical application, constructing a solar-to-hydrogen system is a promising way to realize economic and sustainable H<sub>2</sub> production. The electrolyzer can be driven by a commercial solar panel illuminated under the sunlight (1.43 V) (Figure 5b) with obvious H<sub>2</sub> and O<sub>2</sub> bubbles at the surfaces of both electrodes (Figure 5c), indicating its potential to convert low-voltage electricity generated from solar energy into chemical energy. Besides, the overpotential of 202 mV is also lower than most of the previously reported electrocatalysts (Figure 5d, Table S9, Supporting Information) such as Ir-NSG ( $\eta_{10} = 220$  mV),<sup>[44]</sup> NiMoO<sub>x</sub>/NiMoS ( $\eta_{10} = 230$  mV),<sup>[45]</sup> Co<sub>3</sub>Mo ( $\eta_{10} = 250$  mV),<sup>[46]</sup> (Ru-Co)O<sub>x</sub> ( $\eta_{10} = 258$  mV),<sup>[47]</sup> Co<sub>0.85</sub>Se<sub>1-x</sub>@C ( $\eta_{10} = 260$  mV),<sup>[48]</sup> P-MoP/MoN ( $\eta_{10} = 310$  mV),<sup>[49]</sup> NiS<sub>0.5</sub>Se<sub>0.5</sub> ( $\eta_{10} = 320$  mV),<sup>[50]</sup> CoFeO@BP ( $\eta_{10} = 350$  mV),<sup>[51]</sup> and Ni/Ni(OH)<sub>2</sub> ( $\eta_{10} = 360$  mV).<sup>[52]</sup>

### 3. Conclusion

In summary, we developed a carbonate-hydroxide induced MOF transformation strategy to in situ grow 10–40 nm porous, honeycomb-like NiCoP nanoplates on Ni foam for high-performance, pH-universal hydrogen evolution reaction. The resultant NiCoP catalyst exhibits a highly 2D nanoporous network in which 20–50 nm, well-crystalline nanoparticles were interconnected with each other closely. Prominent pH-universal

HER performance with overpotentials of 98, 105, and 97 mV in 1 M KOH, 0.5 M H<sub>2</sub>SO<sub>4</sub>, and 1 M phosphate buffer solution (PBS) at the current density of 10 mA cm<sup>-2</sup> has been achieved, respectively. The corresponding full water-splitting electrolyzer constructed from the 2D porous NiCoP cathode requires only a cell voltage of 1.43 V at 10 mA cm<sup>-2</sup> owing to a low overpotential of 202 mV, superior to most recently reported electrocatalysts. This work may open up a new avenue on the rational design of nonprecious, pH-universal electrocatalyst to convert plentiful solar energy into H<sub>2</sub> energy for large-scale hydrogen production, and also provides a fundamental insight into the correlation between the porous structure and catalytic activity.

## 4. Experimental Section

**Materials:** Cobalt nitrate hexahydrate (Co(NO<sub>3</sub>)<sub>2</sub>·6H<sub>2</sub>O), Nickel nitrate hexahydrate (Ni(NO<sub>3</sub>)<sub>2</sub>·6H<sub>2</sub>O), urea (CO(NH<sub>2</sub>)<sub>2</sub>), ammonium fluoride (NH<sub>4</sub>F), KOH, sodium hypophosphite (NaH<sub>2</sub>PO<sub>2</sub>), 1,4-Diazabicyclo[2.2.2]octane (DABCO), N,N-dimethylformamide (DMF, C<sub>3</sub>H<sub>7</sub>NO, ≥99.8%), and ethanol (C<sub>2</sub>H<sub>5</sub>OH) were purchased from Sinopharm Chemical Reagent Co., Ltd. 1,4-dicarboxybenzene (HBDC), pyridine, and RuO<sub>2</sub> were purchased from Alfa Aesar. Ni Foam and Pt/C were purchased from Shanghai Hesun Electric Co., Ltd. There were no further purification of the reagents and solvents. Deionized water was used in the experiments.

**Preparation of the NCCH@Ni Foam:** The Co–Ni-carbonates hydroxide on Ni foam were prepared by a hydrothermal reaction.<sup>[28]</sup> Briefly, a piece of commercial Ni Foam (2 cm × 4 cm) was cleaned by acetone and deionized (DI) water with the assistance of ultrasonication for 15 min.<sup>[53]</sup> Then, the NF was sonicated in HCl (2 M) for 2 min to remove the oxide layers on the surface, followed by rinsing with DI water. The treated Ni Foam was dried and weighed. And 2 mmol Ni(NO<sub>3</sub>)<sub>2</sub>·6H<sub>2</sub>O, 2 mmol Co(NO<sub>3</sub>)<sub>2</sub>·6H<sub>2</sub>O, 16 mmol of NH<sub>4</sub>F and 20 mmol of CO(NH<sub>2</sub>)<sub>2</sub> were dissolved in 72 mL deionized water. After 30 min of vigorous stirring at ambient temperature, the as-prepared solution was transferred into teflon-lined autoclave and the pre-treated Ni Foam added. The autoclave was sealed and heated up to 100 °C for 4 h. Afterward the system was allowed to cool down to room temperature, the NiCo precursor/NF were obtained by washing several times with deionized water and ethanol, then dried at 60 °C overnight for further use.

**Preparation of the Ni-MOF@NCCH@Ni Foam (MOF/NiCo):** For the preparation of MOF/NiCo, first 0.35 mmol of Ni(NO<sub>3</sub>)<sub>2</sub>·6H<sub>2</sub>O, 0.35 mmol of HBDC, and 0.875 mmol DABCO were dissolved in 70 mL DMF under ultrasonic for 15 min. The 0.3 mL pyridine was dropped to the former solution under magnetic stirring for 10 min to obtain the blue solution A. After that, the solution A was transferred into teflon-lined autoclave and the NCCH/Ni Foam added. The autoclave was sealed and heated up to 80 °C for 12 h. The color of the Ni foam was changed from pink to green after hydrothermal reaction and was then washed with ethanol and finally dried at 60 °C for 12 h to obtain the precursor.

**Preparation of the MOF/NiCo-325:** The as-prepared Ni foam coated with Ni-MOF@Ni–Co-carbonates hydroxide was loaded in porcelain boats with NaH<sub>2</sub>PO<sub>2</sub> placed upstream, and then heated to 325 °C for 2 h with a heating rate of 5 °C min<sup>-1</sup> and then cooled to room temperature to yield a black product MOF/NiCo-325.

**Preparation of the Ni-325 and NiCo-325:** The Ni-325 (NiCo-325) were prepared through the pyrolysis of Ni-MOF/Ni Foam (Ni–Co-carbonates hydroxide/Ni Foam) with NaH<sub>2</sub>PO<sub>2</sub> placed upstream at 325 °C for 2 h under Ar atmosphere. And then cooled to room temperature, and a black product Ni-325 (NiCo-325) was obtained.

**Materials Characterization:** Powder XRD pattern was obtained on a Bruker D8 Advance diffractometer with Cu-Kα radiation λ = 0.15406 nm. Raman spectra were collected on a Renishaw in via spectrometer with an excitation laser wavelength of 457.9 nm. Fourier transform infrared spectrum was measured from a NICOLETIS50 spectrometer. X-ray

photoelectron spectra (XPS, PHI 5000C EACA system XPS using an Mg Kα) was performed to obtain the elemental composition and chemical state of the materials. The morphologies of as-obtained products were observed by SEM (Hitachi S-4800 electron microscopy) at an accelerating voltage of 5 kV. TEM and HRTEM were performed on a JEM-2100F Field Emission Electron microscope, respectively.

**Electrochemical Measurement:** All electrochemical measurements were carried out on the electrochemical workstation (CHI 760 E). The as-prepared materials (MOF/NiCo-325 on Ni Foam (1 × 1.5 cm), catalyst loading: ≈2.5 mg cm<sup>-2</sup>), a graphite rod, and saturated calomel electrode (SCE) were used as the working electrode, the counter electrode, and the reference electrode, respectively.<sup>[54]</sup> Before the electrochemical measurements, the electrolyte in 1 M KOH (pH = 13.8), 0.5 M H<sub>2</sub>SO<sub>4</sub> (pH = 0.3), and 1 M PBS (pH = 7.1) was purged with N<sub>2</sub> for 1 h to remove the dissolved gases completely. All the potentials were quoted with respect to the reversible hydrogen electrode (RHE) through  $E_{\text{RHE}} = E_{\text{SCE}} + 0.059 \times \text{pH} + 0.244 \text{ V}$ .<sup>[55]</sup> Cyclic voltammetry (CV) was conducted at a scan rate of 100 mV s<sup>-1</sup> to activate the catalysts. The linear sweep voltammograms (LSV) curves were collected at a sweep rate of 1 mVs<sup>-1</sup> with 90% IR compensation. Long-term stability tests were carried out by using chronoamperometry measurement method. Electrochemical impedance spectroscopy (EIS) was performed by applying an AC voltage with 5 mV amplitude at the overpotentials of –0.11 V (vs RHE) for HER from 0.1 Hz to 100 kHz in the acidic, neutral, and alkaline electrolytes. Cyclic voltammetry was conducted to probe the double-layer capacitor (C<sub>dl</sub>) to calculate the ESCA, and the scan rates were 20–200 mV s<sup>-1</sup>. The above tests were all performed at room temperature (25 °C). In overall water splitting tests, the MOF/NiCo-325 and Fe-CoP/NF were used as cathode and anode respectively in a two-electrode reactor for overall water splitting. The loadings of RuO<sub>2</sub>, Pt/C on the Ni Foam were about 2.5 mg cm<sup>-2</sup>.

## Supporting Information

Supporting Information is available from the Wiley Online Library or from the author.

## Acknowledgements

This work was financially supported by the National Natural Science Foundation of China (Grant Nos. 52171203 and 51872051), the National Key Research and Development Program of China (Grant No. 2021YFB2400400), the Natural Science Foundation of Jiangsu Province (Grants No. BK20211516), the State Key Laboratory of New Ceramic and Fine Processing Tsinghua University (Grant No. KF202102), and the Fundamental Research Funds for the Central Universities (Grant No. 2242022R10090).

## Conflict of Interest

The authors declare no conflict of interest.

## Data Availability Statement

Research data are not shared.

## Keywords

honeycomb-like networks, hydrogen evolution, NiCoP nanoplates, pH-universal electrocatalysts, water-splitting

Received: May 6, 2022  
Published online: July 1, 2022



- [1] Y. Li, X. F. Wei, L. Chen, J. L. Shi, *Angew. Chem., Int. Ed.* **2021**, *60*, 19550.
- [2] Z. Z. Liang, H. Y. Wang, H. Q. Zheng, W. Zhang, R. Cao, *Chem. Soc. Rev.* **2021**, *50*, 2540.
- [3] I. S. Amiin, Z. H. Pu, Z. H. Pu, X. B. Liu, K. A. Owusu, H. G. R. Monestel, F. O. Boakye, H. Zhang, S. C. Mu, *Adv. Funct. Mater.* **2017**, *27*, 1702300.
- [4] N. N. Xu, Y. X. Zhang, J. L. Qiao, Y. Y. Liu, J. L. Qiao, *Nano Energy* **2019**, *57*, 176.
- [5] S. Lu, Y. Zhang, F. L. Lou, K. Guo, Z. X. Yu, *Appl. Surf. Sci.* **2022**, *579*, 152234.
- [6] S. Anantharaj, S. Kundu, S. Noda, *J. Mater. Chem. A* **2020**, *8*, 4174.
- [7] W. F. Chen, J. T. Muckerman, E. Fujita, *Chem. Commun.* **2013**, *49*, 8896.
- [8] Y. L. Zhu, Q. Lin, Y. J. Zhong, H. A. Tahini, Z. P. Shao, H. T. Wang, *Energy Environ. Sci.* **2020**, *13*, 3361.
- [9] B. Ma, Z. C. Yang, Y. T. Chen, Z. H. Yuan, *Nano Res.* **2019**, *12*, 375.
- [10] P. Z. Chen, K. Xu, Z. W. Fang, Y. Tong, J. C. Wu, X. L. Lu, X. Peng, H. Ding, C. Z. Wu, Y. Xie, *Angew. Chem., Int. Ed.* **2015**, *54*, 14710.
- [11] A. K. Tareen, G. S. Priyanga, K. Khan, E. Pervaiz, T. Thomas, M. H. Yang, *ChemSusChem* **2019**, *12*, 3941.
- [12] B. Kim, T. Kim, K. Lee, J. H. Li, *ChemElectroChem* **2020**, *7*, 3578.
- [13] P. Liu, J. A. Rodriguez, *J. Am. Chem. Soc.* **2005**, *127*, 14871.
- [14] X. Q. Xie, J. P. Liu, C. N. Gu, J. J. Li, Y. Zhao, C. S. Liu, *J. Energy Chem.* **2022**, *64*, 503.
- [15] Y. M. Shi, B. Zhang, *Chem. Soc. Rev.* **2016**, *45*, 1529.
- [16] S. Carencu, D. Portehault, C. Boissière, N. Mézailles, C. Sanchez, *Chem. Rev.* **2013**, *113*, 7981.
- [17] B. Kim, T. Kim, K. Lee, J. H. Li, *ChemElectroChem* **2020**, *7*, 3578.
- [18] Y. F. Zeng, Y. Y. Wang, G. Huang, C. Chen, L. L. Huang, R. Chen, S. Y. Wang, *Chem. Commun.* **2018**, *54*, 1465.
- [19] Z. G. Ye, T. Li, G. Ma, Y. H. Dong, X. L. Zhou, *Adv. Funct. Mater.* **2017**, *27*, 1704083.
- [20] C. L. Tan, X. H. Cao, X. J. Wu, Q. Y. He, J. Yang, X. Zhang, J. Chen, W. Zhao, S. K. Han, G. H. Nam, M. Sindoro, H. Zhang, *Chem. Rev.* **2017**, *117*, 6225.
- [21] H. Zhang, J. Y. Xu, Y. W. Jin, Y. L. Tong, Q. Y. Lu, F. Gao, *Chem. - Eur. J.* **2018**, *24*, 14522.
- [22] T. N. Tran, H. Y. Lee, J. D. Park, T. H. Kang, B. J. Lee, J. S. Yu, *ACS Appl. Energy Mater.* **2020**, *3*, 6310.
- [23] S. Li, C. Cheng, H. W. Liang, X. L. Feng, A. Thomas, *Adv. Mater.* **2017**, *29*, 1700707.
- [24] H. F. Liang, A. N. Gandi, D. H. Anjum, X. B. Wang, U. Schwingenschlögl, H. N. Alshareef, *Nano Lett.* **2016**, *16*, 7718.
- [25] X. D. Lv, X. T. Li, C. Yang, X. Q. Ding, Y. F. Zhang, Y. Z. Zheng, S. Q. Li, X. N. Sun, X. Tao, *Adv. Funct. Mater.* **2020**, *30*, 1910830.
- [26] Y. J. Li, H. C. Zhang, M. Jiang, Y. Kuang, X. M. Sun, X. Duan, *Nano Res.* **2016**, *9*, 2251.
- [27] R. Boppella, J. W. Tan, W. Yang, J. Moon, *Adv. Funct. Mater.* **2019**, *29*, 1807976.
- [28] Z. C. Cai, A. P. Wu, H. J. Yan, Y. L. Xiao, C. F. Chen, C. G. Tian, L. Wang, R. H. Wang, H. G. Fu, *Nanoscale* **2018**, *10*, 7619.
- [29] J. Wang, F. Xu, H. Y. Jin, Y. Q. Chen, Y. Wang, *Adv. Mater.* **2017**, *29*, 1605838.
- [30] L. Y. Wang, H. Xu, J. M. Yao, Q. C. Zhang, *Coord. Chem. Rev.* **2019**, *398*, 213016.
- [31] Y. F. Lin, H. Wan, D. Wu, G. Chen, N. Zhang, X. H. Liu, J. H. Li, Y. J. Cao, G. Z. Qiu, R. Z. Ma, *J. Am. Chem. Soc.* **2020**, *142*, 7317.
- [32] J. Wei, Y. X. Hu, Y. Liang, B. Kong, Z. F. Zheng, J. Zhang, S. P. Jiang, Y. X. Zhao, H. T. Wang, *J. Mater. Chem. A* **2017**, *5*, 10182.
- [33] Q. X. Yang, R. Lu, S. S. Ren, C. T. Chen, Z. J. Chen, X. Y. Yang, *Chem. Eng. J.* **2018**, *348*, 202.
- [34] W. Sun, G. Q. Ning, T. Wei, Q. Zhang, R. F. Zhang, L. J. Zhi, *Adv. Funct. Mater.* **2012**, *22*, 2632.
- [35] K. Rui, G. Q. Zhao, Y. P. Chen, Y. Lin, Q. Zhou, J. Y. Chen, J. X. Zhu, W. P. Sun, W. Huang, S. X. Dou, *Adv. Funct. Mater.* **2018**, *28*, 1801554.
- [36] H. Y. Zhao, D. D. Yin, J. W. Wang, Y. S. Zheng, Y. P. Du, *J. Mater. Chem. A* **2019**, *7*, 20176.
- [37] X. Zhang, Y. F. Zhao, Y. F. Zhao, X. D. Jia, Y. X. Zhao, L. Shang, Q. Wang, G. I. N. Waterhouse, L. Z. Wu, C. H. Tung, T. R. Zhang, *Adv. Energy Mater.* **2018**, *8*, 1702780.
- [38] E. P. Cao, Z. M. Chen, H. Wu, P. Yu, Y. Wang, F. Xiao, S. Chen, S. C. Du, Y. Xie, Y. Q. Wu, Z. Y. Ren, *Angew. Chem., Int. Ed.* **2020**, *59*, 4154.
- [39] X. M. Zhang, A. P. Wu, X. W. Wang, C. G. Tian, R. Y. An, H. G. Fu, *J. Mater. Chem. A* **2018**, *6*, 17905.
- [40] M. Kim, M. Anjum, M. Choi, H. Y. Jeong, S. H. Choi, N. J. Park, J. S. Lee, *Adv. Funct. Mater.* **2020**, *30*, 2002536.
- [41] Z. H. Pu, I. S. Amiin, Z. K. Kou, W. Q. Li, S. C. Mu, *Angew. Chem., Int. Ed.* **2017**, *56*, 11559.
- [42] T. Liu, P. Li, N. Yao, G. Z. Cheng, S. I. Chen, W. Luo, Y. D. Yin, *Angew. Chem., Int. Ed.* **2019**, *58*, 4679.
- [43] L. M. Cao, Y. W. Hu, Y. W. Hu, S. F. Tang, A. Iljin, J. W. Wang, Z. M. Zhang, T. B. Lu, *Adv. Sci.* **2018**, *5*, 1800949.
- [44] Q. L. Wang, C. Q. Xu, W. Liu, S. F. Hung, H. B. Yang, J. J. Gao, W. Z. Cai, H. M. Chen, J. Li, B. Liu, *Nat. Commun.* **2020**, *11*, 4246.
- [45] P. L. Zhai, Y. X. Zhang, Y. Z. Wu, J. F. Gao, B. Zhang, S. Y. Cao, Y. T. Zhang, Z. W. Li, L. C. Sun, J. G. Hou, *Nat. Commun.* **2020**, *11*, 5462.
- [46] H. Shi, Y. T. Zhou, R. Q. Yao, W. B. Wan, X. Ge, W. Zhang, Z. Wen, X. Y. Lang, W. T. Zheng, Q. Jiang, *Nat. Commun.* **2020**, *11*, 2940.
- [47] C. Wang, L. M. Qi, *Angew. Chem., Int. Ed.* **2020**, *59*, 17219.
- [48] L. Zhang, C. J. Lu, F. Ye, R. L. J. Pang, Y. Liu, Z. Y. Wu, Z. P. Shao, Z. M. Sun, L. F. Hu, *Adv. Mater.* **2021**, 2007523.
- [49] Y. Gu, A. P. Wu, Y. Q. Jiao, H. R. Zheng, X. Q. Wang, Y. Xie, L. Wang, C. G. Tian, H. G. Fu, *Angew. Chem., Int. Ed.* **2020**, *60*, 6673.
- [50] Y. Wang, X. P. Li, M. M. Zhang, Y. G. Zhou, D. W. Rao, C. Zhong, J. F. Zhang, X. P. Han, W. B. Hu, Y. C. Zhang, K. Zaghi, Y. S. Wang, Y. Deng, *Adv. Mater.* **2020**, *32*, 2000231.
- [51] X. Y. Li, L. P. Xiao, L. Zhou, Q. C. Xu, J. Weng, X. Jun, L. Bin, *Angew. Chem., Int. Ed.* **2020**, *59*, 21106.
- [52] L. Dai, Z. N. Chen, L. X. Li, P. Q. Yin, Z. Q. Liu, H. Zhang, *Adv. Mater.* **2020**, *32*, 1906915.
- [53] L. B. Wu, L. Yu, F. H. Zhang, B. McElhenny, D. Luo, A. Karim, S. Chen, Z. F. Ren, *Adv. Funct. Mater.* **2020**, *31*, 2006484.
- [54] H. J. Yan, Y. Q. Jiao, Y. Q. Jiao, A. P. Wu, C. G. Tian, X. M. Zhang, L. Wang, Z. Y. Ren, H. G. Fu, *Chem. Commun.* **2016**, *52*, 9530.
- [55] G. C. Yang, Y. Q. Jiao, H. J. Yan, Y. Xie, A. P. Wu, X. Dong, D. Z. Guo, H. G. Fu, *Adv. Mater.* **2020**, *32*, 2000455.